The Astrophysical Journal, 716:269–280, 2010 June 10 doi:10.1088/0004-637X/716/1/269

THE LICK AGN MONITORING PROJECT: THE M_{BH}–σ_* RELATION FOR REVERBERATION-MAPPED ACTIVE GALAXIES

Jong-Hak Woo[1,2,12], Tommaso Treu[3,13], Aaron J. Barth[4], Shelley A. Wright[5,12], Jonelle L. Walsh[4], Misty C. Bentz[4,12], Paul Martini[6], Vardha N. Bennert[3], Gabriela Canalizo[7], Alexei V. Filippenko[5], Elinor Gates[8], Jenny Greene[9,14], Weidong Li[5], Matthew A. Malkan[2], Daniel Stern[10], and Takeo Minezaki[11]

[1] Astronomy Program, Department of Physics and Astronomy, Seoul National University, Seoul 151-742, Republic of Korea; woo@astro.snu.ac.kr
[2] Department of Physics, University of California, Los Angeles, CA 90024, USA
[3] Department of Physics, University of California, Santa Barbara, CA 93106, USA
[4] Department of Physics and Astronomy, 4129 Frederick Reines Hall, University of California, Irvine, CA 92697-4575, USA
[5] Department of Astronomy, University of California, Berkeley, CA 94720-3411, USA
[6] Department of Astronomy, and Center for Cosmology and Astroparticle Physics, The Ohio State University, 140 West 18th Avenue, Columbus, OH 43210, USA
[7] Department of Physics and Astronomy, University of California, Riverside, CA 92521, USA
[8] Lick Observatory, P.O. Box 85, Mount Hamilton, CA 95140, USA
[9] Department of Astrophysical Sciences, Princeton University, Princeton, NJ 08544, USA
[10] Jet Propulsion Laboratory, California Institute of Technology, MS 169-527, 4800 Oak Grove Drive, Pasadena, CA 91109, USA
[11] Institute of Astronomy, School of Science, University of Tokyo, 2-21-1 Osawa, Mitaka, Tokyo 181-0015, Japan
Received 2009 December 9; accepted 2010 April 10; published 2010 May 17

ABSTRACT

To investigate the black hole mass versus stellar velocity dispersion (M_{BH}–σ_*) relation of active galaxies, we measured the velocity dispersions of a sample of local Seyfert 1 galaxies, for which we have recently determined black hole masses using reverberation mapping. For most objects, stellar velocity dispersions were measured from high signal-to-noise ratio optical spectra centered on the Ca II triplet region (∼8500 Å), obtained at the Keck, Palomar, and Lick Observatories. For two objects, in which the Ca II triplet region was contaminated by nuclear emission, the measurement was based on high-quality *H*-band spectra obtained with the OH-Suppressing Infrared Imaging Spectrograph at the Keck-II telescope. Combining our new measurements with data from the literature, we assemble a sample of 24 active galaxies with stellar velocity dispersions *and* reverberation-based black hole mass measurements in the range of black hole mass $10^6 < M_{BH}/M_\odot < 10^9$. We use this sample to obtain reverberation-mapping constraints on the slope and intrinsic scatter of the M_{BH}–σ_* relation of active galaxies. Assuming a constant virial coefficient f for the reverberation-mapping black hole masses, we find a slope $\beta = 3.55 \pm 0.60$ and the intrinsic scatter $\sigma_{int} = 0.43 \pm 0.08$ dex in the relation $\log(M_{BH}/M_\odot) = \alpha + \beta \log(\sigma_*/200\ \mathrm{km\ s^{-1}})$, which are consistent with those found for quiescent galaxies. We derive an updated value of the virial coefficient f by finding the value which places the reverberation masses in best agreement with the M_{BH}–σ_* relation of quiescent galaxies; using the quiescent M_{BH}–σ_* relation determined by Gültekin et al., we find $\log f = 0.72^{+0.09}_{-0.10}$ with an intrinsic scatter of 0.44 ± 0.07 dex. No strong correlations between f and parameters connected to the physics of accretion (such as the Eddington ratio or line-shape measurements) are found. The uncertainty of the virial coefficient remains one of the main sources of the uncertainty in black hole mass determinations using reverberation mapping, and therefore also in single-epoch spectroscopic estimates of black hole masses in active galaxies.

Key words: galaxies: active – galaxies: kinematics and dynamics – galaxies: nuclei – galaxies: Seyfert

Online-only material: color figures

1. INTRODUCTION

In the past decade, supermassive black holes have been found to be virtually ubiquitous at the centers of local quiescent galaxies (for reviews, see Kormendy 2004; Ferrarese & Ford 2005). Remarkably, the mass of the central black hole (M_{BH}) correlates with the global properties of their host spheroids, primarily the stellar velocity dispersion (σ_*; Ferrarese & Merritt 2000; Gebhardt et al. 2000a). This M_{BH}–σ_* relation is believed to be of fundamental importance, providing one of the strongest empirical links between galaxy formation/evolution and nuclear activity. Measuring the slope and scatter of the relation, and any possible dependence on additional parameters, it is essential to make progress in our understanding of the co-evolution of galaxies and black holes.

One key open question is whether active galactic nuclei (AGNs) share the same M_{BH}–σ_* relation as quiescent galaxies, as would be expected if the relation were universal and nuclear activity were just a random transient phase. Initial studies using several reverberation-mapped Seyfert 1 galaxies show that the M_{BH}–σ_* relation of active galaxies is consistent with that of quiescent galaxies (Gebhardt et al. 2000b; Ferrarese et al. 2001). Other studies using larger samples with single-epoch black hole masses suggest that the slope of the relation may be different than that of quiescent galaxies, albeit at low significance (e.g., Greene & Ho 2006; Shen et al. 2008). However, these later studies rely on an indirect estimator of black hole mass, based on the kinematics and size of the broad-line region (BLR) as inferred from single-epoch spectra. The method works as follows: the broad-line profile gives a characteristic velocity scale ΔV (measured from either line dispersion, σ_{line}, or the full width at half-maximum intensity, V_{FWHM}); the average size of the BLR (R_{BLR}) is determined from the empirical correlation

[12] Hubble Fellow.
[13] Sloan Fellow; Packard Fellow.
[14] Princeton-Carnegie Fellow.

with optical luminosity (Wandel et al. 1999; Kaspi et al. 2005; Bentz et al. 2009a); and the black hole mass is obtained as

$$M_{\rm BH} = f\frac{(\Delta V)^2 R_{\rm BLR}}{G}, \quad (1)$$

where G is the gravitational constant and f is a virial coefficient that depends on the kinematics and the geometry of the BLR. Although single-epoch mass estimates are believed to be accurate to ∼0.5 dex (e.g., Vestergaard & Peterson 2006), it is hard to quantify precisely their uncertainty and any possible biases (Marconi et al. 2008). Thus, the slope and intrinsic scatter of the $M_{\rm BH}$–σ_* relation of active galaxies remain highly uncertain.

Multi-epoch data provide direct measurements of the BLR size via reverberation-mapping time lags ($R_{\rm BLR} = c\tau$, where c is the speed of light and τ is the measured reverberation time scale), and more secure measurements of the broad-line kinematics as determined from the variable component of the broad lines (Peterson et al. 2004). Onken et al. (2004) combined reverberation black hole masses with measurements of stellar velocity dispersion for 14 objects to measure the slope of the $M_{\rm BH}$–σ_* relation, showing that AGNs and quiescent galaxies lie on the same $M_{\rm BH}$–σ_* relation for an appropriate choice of the virial coefficient ($f = 5.5 \pm 1.8$).[15] Remarkably, the scatter in $M_{\rm BH}$ relative to the $M_{\rm BH}$–σ_* relation is found to be less than a factor of 3. Unfortunately, their sample is very small (14 objects) and covers a limited dynamic range ($6.2 < \log M_{\rm BH} < 8.4$), making it difficult to simultaneously measure the intrinsic scatter and the slope and investigate any trends with black hole mass, or with other properties of the nucleus or the host galaxy (cf. Collin et al. 2006). Under the assumption that the relations should be the same for active and quiescent galaxies, the Onken et al. (2004) study provides some information on the geometry of the BLR, an absolute normalization of reverberation black hole mass, and an upper limit to the intrinsic scatter in the virial coefficient. Since the reverberation-mapped AGN sample is the "gold standard" used to calibrate all single-epoch mass estimates (e.g., Woo & Urry 2002; Vestergaard et al. 2002; McLure & Jarvis 2002; Vestergaard & Peterson 2006; McGill et al. 2008; Shen et al. 2008), this comparison is effectively a crucial link in establishing black hole masses for all AGNs across the universe and for all evolutionary studies (e.g., McLure & Dunlop 2004; Woo et al. 2006, 2008; Peng et al. 2006a, 2006b; Netzer et al. 2007; Bennert et al. 2010; Jahnke et al. 2009; Merloni et al. 2010). In this paper, we present new measurements of host-galaxy velocity dispersion obtained from deep, high-resolution spectroscopy at the Keck, Palomar, and Lick Observatories. The new measurements are combined with existing data (e.g., Onken et al. 2004; Nelson et al. 2004; Watson et al. 2008) and with recently determined black hole masses from reverberation mapping (Bentz et al. 2009b) to construct the $M_{\rm BH}$–σ_* relation of broad-lined AGNs for an enlarged sample of 24 objects. For the first time, we are able to determine *simultaneously* the intrinsic scatter and the slope of the $M_{\rm BH}$–σ_* relation of active galaxies. Also, by forcing the slope of the $M_{\rm BH}$–σ_* relation to match that of quiescent galaxies, we determine the average virial coefficient and its non-zero intrinsic scatter. Finally, we study the residuals from the determined $M_{\rm BH}$–σ_* relation to investigate possible trends in virial coefficient with properties of the active nucleus.

[15] Note that the virial coefficient, $\langle f \rangle$, is 5.5 when the line dispersion ($\sigma_{\rm line}$) is used. If $V_{\rm FWHM}$ is used, $\langle f \rangle$ has to be properly scaled depending on the $V_{\rm FWHM}/\sigma_{\rm line}$ ratio. See Onken et al. (2004) and Collin et al. (2006) for details.

The paper is organized as follows. In Section 2, we describe the observations and data reduction of the optical and the near-infrared (near-IR) data. New velocity dispersion measurements are presented in Section 3, along with a summary of previous measurements in the literature. In Section 4, we investigate the $M_{\rm BH}$–σ_* relation of the present-day AGNs, and determine the virial coefficient in measuring $M_{\rm BH}$. Discussion and summary follow in Sections 5 and 6, respectively.

2. OBSERVATIONS

The Lick AGN Monitoring Project (LAMP) was designed to determine the reverberation time scales of a sample of 13 local Seyfert 1 galaxies, particularly with low black hole masses ($< 10^7\ M_\odot$). NGC 5548, the best-studied reverberation target, was included in our Lick monitoring campaign to test the consistency of our results with previous measurements. The 64-night spectroscopic monitoring campaign, along with nightly photometric monitoring, was carried out using the 3 m Shane reflector at Lick Observatory and other, smaller telescopes. The detailed photometric and spectroscopic results are described by Walsh et al. (2009), Bentz et al. (2009b), and Bentz et al. (2010), respectively. In summary, nine objects including NGC 5548 showed enough variability in the optical continuum and the Hβ line to obtain the reverberation time scales. This significantly increases the size of the reverberation sample, particularly for this low-mass range.

For the LAMP sample of 13 objects, we carried out spectroscopy using various telescopes, to measure stellar velocity dispersions. Here, we describe each observation and the data-reduction procedures. The date, total exposure time, and other parameters for each observation are listed in Table 1.

2.1. Optical Data

2.1.1. Palomar Observations

Observations of six galaxies were obtained with the Double Spectrograph (DBSP; Oke & Gunn 1982) at the Palomar Hale 5 m telescope (P200). A 2″-wide slit was used, along with the D68 dichroic. On the red side of the spectrograph, we used a 1200 lines mm^{-1} grating blazed at 9400 Å, covering the wavelength range 8330–8960 Å at an instrumental dispersion of $\sigma_i \approx 30.4$ km s^{-1}.

Each galaxy was observed with the slit oriented approximately at the parallactic angle (Filippenko 1982) for the midpoint of the observation. Typically, two or three exposures were taken for each galaxy to aid in cosmic-ray removal. Flux standards and a range of velocity template stars (primarily K-type giants) were observed during each night.

2.1.2. Lick Observations

Mrk 290 was observed with the Kast Double Spectrograph (Miller & Stone 1993) at the Shane 3 m telescope at Lick Observatory on 2008 April 13 (UT dates are used throughout this paper), during our AGN monitoring campaign. For these observations, we used the D55 dichroic and the 830/8460 grating on the red side of the spectrograph, covering the wavelength range 7570–9620 Å at a scale of 1.7 Å pixel^{-1}. A 2″-wide slit was used and oriented at the parallactic angle for the midpoint of the exposure sequence, and the instrumental dispersion was $\sigma_i \approx 59$ km s^{-1} at 8600 Å. We obtained four 900 s exposures of Mrk 290 with this setup, along with short exposures of three velocity template stars and the flux standard star BD +28°4211.

Table 1
Observation Log

Galaxy	Telescope/Instrument	UT Date	Exposure Time (s)	P.A. (deg)	Airmass	S/N
Arp 151	P200/DBSP	2003 Jan 28	5400	210	1.10	79
IC 1198 (Mrk 871)	Keck/ESI	2008 Mar 2	900	285	1.25	87
IC 4218	P200/DBSP	2003 Jun 2	3600	5	1.23	61
MCG −06-30-15	P200/DBSP	2003 Jun 1	5400	10	2.70	112
Mrk 1310	Keck/ESI	2008 Mar 2	1800	323	1.19	84
Mrk 142	Keck/OSIRIS	2009 May 3	3600	0	1.19	17
Mrk 202	Keck/ESI	2008 Mar 2	1200	204	1.32	73
Mrk 290	Lick/Kast	2008 Apr 13	3600	168	1.07	27
NGC 4253 (Mrk 766)	P200/DBSP	2001 Jun 26	1200	220	1.60	63
	Keck/OSIRIS	2009 May 3	3600	0	1.03	67
NGC 4748	Keck/ESI	2004 Feb 17	1200	25	1.23	160
	Keck/OSIRIS	2009 May 4	5400	0	1.37	61
NGC 5548	P200/DBSP	2003 Jun 1	1800	59	1.06	100
NGC 6814	P200/DBSP	2003 Jun 1	3600	0	1.38	165
SBS 1116+583A	Keck/ESI	2008 Mar 2	1800	216	1.40	53

Notes. For OSIRIS observations, the position angle (P.A.) refers to the direction of the long axis of the IFU; for all other observations, it refers to the slit P.A.. The S/N refers to the signal-to-noise ratio per pixel in the extracted spectra, at ∼8400–8700 Å for the Ca II triplet spectral region, or at ∼1.47–1.61 μm for the *H*-band spectra.

2.1.3. Keck Observations

Five galaxies were observed with the Echellete Spectrograph and Imager (ESI; Sheinis et al. 2002) at the Keck-II 10 m telescope. In ESI echellette mode, the observations cover 3900–11000 Å in 10 spectral orders at a scale of ∼11.4 km s^{-1} pixel^{-1}. We used a 0.″75-wide slit, giving an instrumental dispersion of $\sigma_i \approx 22$ km s^{-1}.

The slit was oriented at the parallactic angle in all observations. During twilight of each night, we observed flux standards and several velocity template stars with spectral types ranging from G8III to K5III.

2.1.4. Reductions

We reduced the DBSP and Kast data using a series of IRAF[16] scripts. The standard spectroscopic data-reduction procedure, including bias subtraction, flat-fielding, wavelength calibration, spectral extraction, and flux calibration, was performed for each data set. Optimal extraction (Horne 1986) was used for obtaining one-dimensional spectra to achieve maximal signal-to-noise ratio (S/N) on the stellar features. The typical extraction radius was ∼ 2″–3″, which corresponds to a physical radius of ∼1 kpc.

The ESI observations require some special preparation and calibration before they can be combined and used for kinematic analysis. The calibration process undertaken includes the following steps: bias subtraction, flat-fielding, cosmic-ray rejection, wavelength calibration, rectification, and sky subtraction. These steps were performed by the IRAF package `EASI2D`, which was developed by David J. Sand and Tommaso Treu (Sand et al. 2004) for easy extraction of echelle orders. Approximate flux calibration was performed using ESI response curves measured during photometric nights. During wavelength calibration the spectra were rebinned to uniform steps in log λ corresponding to 11.4 km s^{-1}, which is close to the native pixel scale of ESI, thus minimizing covariance between pixels and loss of resolution due to rebinning. The root mean square (rms) residuals in the wavelength solution are much smaller than a pixel (typically 5%) and therefore negligible. Spectral resolution was measured from night-sky lines and from wavelength-calibration lines taken in the same configuration and reduced through the same pipeline to include all instrumental effects. As for the DBSP and Kast data, optimal extraction was used for obtaining one-dimensional spectra. The typical extraction radius of the ESI spectra was ∼1″–1.″5, which corresponds to a physical radius of ∼0.5 kpc at the mean redshift of the observed AGNs.

[16] IRAF is distributed by the National Optical Astronomy Observatory, which is operated by the Association of Universities for Research in Astronomy, Inc., under cooperative agreement with the National Science Foundation.

2.2. Near-infrared Data

2.2.1. Keck Observations

For three galaxies, we obtained *H*-band spectra using the integral-field unit (IFU) OH-Suppressing Infrared Imaging Spectrograph (OSIRIS; Larkin et al. 2006) at the Keck-II telescope, operated with the laser guide-star adaptive optics (LGS-AO) system (Wizinowich et al. 2006). Using the high angular resolution in the AO-corrected data, our goal was to extract the light from an annulus around the nucleus if necessary, by excluding light from the central, AGN-dominated region, similar to what was done by Watson et al. (2008).

The OSIRIS observations were obtained on 2009 May 3 and 4, during the first half of each night. We used the *H* broadband (Hbb) filter and the 0.″1 lenslet scale, giving a field of view of 1.″6 × 6.″4, with spectra covering the range 1473–1803 nm at a spectral resolving power of $R \approx 3800$. The long spatial direction of the IFU was oriented north–south for all observations.

The observing sequence for each galaxy consisted of sets of four exposures. In three exposures, the nucleus of the galaxy was placed on the IFU. Then one sky exposure with an offset of 21″ to the southeast was taken. The three on-source exposures in each set were dithered northward by 0.″6 between exposures. Each individual exposure had a duration of 600 s for NGC 4748, or 300 s for Mrk 142 and Mrk 766, and total on-source exposure times for each source are listed in Table 1. Immediately preceding and following the observation sequence for each galaxy, we observed an A0V star for telluric correction and flux calibration. The A0V stars were observed using a

sequence of two on-source and one off-source exposure, with typical exposure times of 5–10 s. In order to obtain unsaturated exposures of these bright stars, the AO loops were not closed during the star observations. On each night, velocity template stars were also observed, following the same observing sequence as used for the telluric correction stars. We observed several K- and M-type giant stars as velocity templates, and A0V telluric correction stars were also observed close in time and airmass to the velocity template stars.

The nucleus of each galaxy was used as a tip-tilt reference source ($V \approx 15$–16 mag) for the LGS-AO system, and the laser was propagated on-axis for each dithered exposure. It is difficult to quantify the image quality or determine the Strehl ratio in the galaxy exposures, since the galaxy nuclei are not point sources. However, the typical LGS-AO performance for tip-tilt point sources for these similar magnitudes yields *K*-band Strehl ratios of 40%–50% (van Dam et al. 2006, 2007). Therefore, given that the quality of both nights was excellent, we conservatively estimate the *H*-band Strehl ratio to be ∼15%–20% for our galaxy observations.

Prior to this OSIRIS run, the OSIRIS detector temperature had been rising from its previous operating temperature of 68 K. During these two nights, the detector temperature was steady at 74 K, which resulted in a higher level (∼40%) of dark current than normal for OSIRIS. The higher dark current did not significantly impact our observations, since our exposures were not dark or background limited. In the afternoon, multiple dark frames were taken with exposure times matching those of our observations, and were used as part of the sky-subtraction procedure. In addition, a new calibration file for the observing mode with the Hbb filter and 0.″1 scale was taken at a similar operating temperature to ensure a clean spectral extraction process.

2.2.2. Reductions

The data were reduced using the OSIRIS data-reduction pipeline software (Krabbe et al. 2004). In summary, the reduction steps included dark subtraction, cosmic-ray cleaning and glitch identification, extraction of the spectra into a data cube, wavelength calibration, sky subtraction using the offset-sky exposures, correction for atmospheric dispersion, and telluric correction using the extracted spectra of the A0V stars. The OSIRIS pipeline includes an implementation of the scaled sky-subtraction algorithm described by Davies (2007), which provides a more accurate subtraction of the strong *H*-band airglow lines than a direct subtraction of the offset-sky exposure. However, the current implementation of the scaled sky routine left noticeable residuals around the wavelengths of the strongest blended OH features; we further discuss these sky residuals below. Following the sky subtraction and telluric correction, individual exposures were aligned and co-added to create a final data cube for each galaxy.

We extracted one-dimensional spectra from each data cube using rectangular extraction regions. While we had originally planned to extract an annular region around the nucleus in order to avoid the central, AGN-dominated region, we found that in the reduced data the *H*-band stellar absorption features were visible even in the central region of the galaxy, and it did not prove necessary to exclude the central region from the spectral extractions. We experimented with a variety of different extraction-region sizes for each galaxy. Since the galaxy-light profiles were very centrally concentrated, the extracted spectra did not change significantly beyond some extraction aperture size, and in the end we used extraction apertures that were large enough to contain the majority of the detected galaxy light without including unnecessarily large amounts of noise from the surrounding regions. The extraction aperture sizes were 1.″4 × 2.″4, 1.″3 × 3.″4, and 1.″3 × 3.″4, respectively, for Mrk 142, Mrk 766, and NGC 4748. One-dimensional spectra were similarly extracted from the reduced data cubes for the velocity template stars.

As a result of the imperfect sky subtraction mentioned previously, spectral regions around the wavelengths of the brightest OH emission blends were contaminated by noticeable residuals that appeared to affect all pixels on the IFU in a similar fashion. In order to correct for these additive residuals, for each galaxy we extracted spectra from rectangular regions at the outer edges of the IFU where there was very little galaxy continuum detected, with the same number of pixels as the nuclear extraction, and then subtracted these nearly blank-sky spectra from the nuclear spectra. This correction procedure effectively removed the night-sky emission residuals from the galaxy spectra. The procedure was applied for NGC 4748 and Mrk 142, but was not necessary for Mrk 766 since the OH emission-line strengths appeared to be much more stable during the Mrk 766 observations, leading to a cleaner sky subtraction.

3. STELLAR VELOCITY DISPERSIONS

To measure stellar velocity dispersions, we used the Ca II triplet region (rest frame ∼8500 Å) in the optical spectra, and Mg I and the CO line region (rest frame ∼1.5–1.6 μm) in the near-IR spectra. Velocity dispersions were determined by comparing in pixel space the observed galaxy spectra with stellar templates convolved with a kernel representing Gaussian broadening. Velocity template stars of various spectral types were observed with the same instrumental setup at each telescope, minimizing any systematic errors due to the different spectral resolution of various observing modes. The minimum χ^2 fit was performed using the Gauss–Hermite Pixel Fitting software (van der Marel 1994). The merit of fitting in pixel space as opposed to Fourier space is that typical AGN narrow emission lines and any residuals from night-sky subtraction can be easily masked out (e.g., Treu et al. 2004; Woo et al. 2005, 2006), and the quality of the fit can be directly evaluated. We used low-order polynomials (order 2–4) to model the overall shape of the continuum. Extensive and careful comparison was performed using continua with various polynomials, and the measured velocity dispersions based on each continuum fit with various order polynomials are consistent within the errors (see, e.g., Woo et al. 2004, 2005, 2006). Thus, continuum fitting with low-order polynomials does not significantly affect the velocity dispersion measurements.

3.1. Optical Data

For galaxies with optical spectra, we mainly used the strong Ca II triplet lines (8498, 8542, 8662 Å) to measure the stellar velocity dispersions. We used all velocity template stars with various spectral types (G8–K5 giants) observed with the same instrumental setups, in order to account for possible template mismatches. Fits were performed with each template and the mean of these measurements was taken as the final velocity dispersion measurement. The rms scatter around the mean of individual measurements was added in quadrature to the mean of the individual measurement errors from the χ^2 fit. Given the high S/N of the observed spectra, the uncertainties are typically ∼5%.

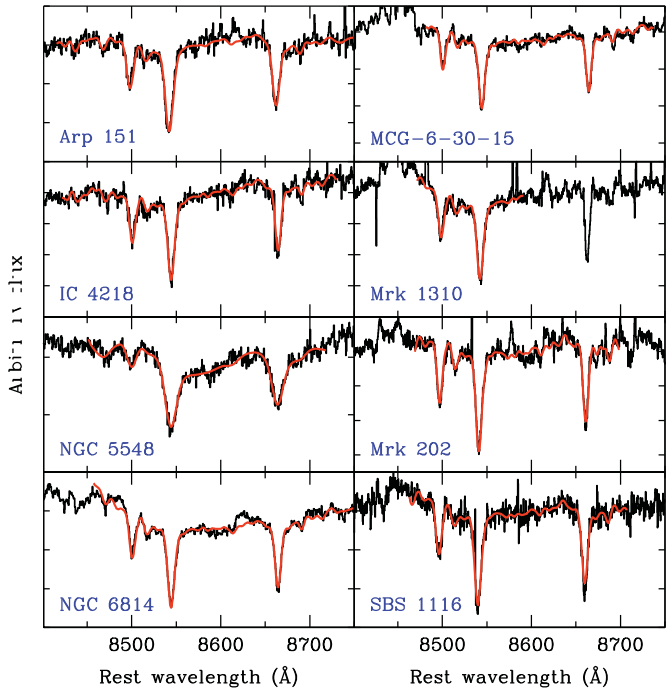

Figure 1. Velocity dispersion measurements using the Palomar DBSP and the Keck ESI spectra. The region including the main stellar features around the Ca II triplet is shown together with the best-fit template (thick red line).

(A color version of this figure is available in the online journal.)

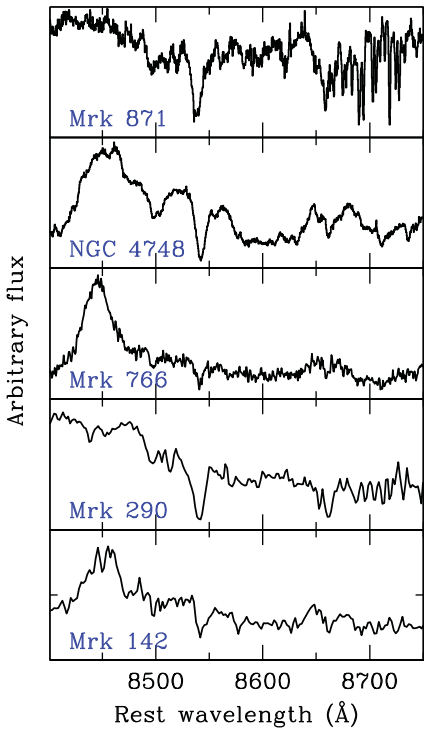

Figure 2. Galaxies with contaminated stellar lines. These galaxies clearly show the Ca II triplet lines; however, due to AGN contamination, the line profiles are asymmetric. Also, the presence of various AGN emission features complicates continuum subtraction. The spectra for the first three objects (Mrk 871, NGC 4748, and Mrk 766) are from Palomar DBSP data. The data for Mrk 290 data were obtained at the Lick telescope, and Mrk 142 data are from SDSS.

(A color version of this figure is available in the online journal.)

We were able to measure the stellar velocity dispersion of eight objects: SBS 1116+538A, Arp 151, Mrk 1310, Mrk 202, IC 4218, NGC 5548, NGC 6814, and MCG −6-30-15. Among these, IC 4218 and MCG −6-30-15 were excluded in the M_{BH}–σ_* relation analysis since we were not able to measure the reverberation time scales (Bentz et al. 2009b). Figure 1 shows examples of the best-fit template along with the observed galaxy spectra. Our measurements based on high-quality data are generally consistent within the errors with previous measurements from the literature for these galaxies, although many of the previously existing measurements had very large uncertainties (see Section 3.3 below).

In the case of the other five objects (Mrk 871, NGC 4748, Mrk 766, Mrk 290, and Mrk 142), the Ca II triplet lines were contaminated by AGN emission lines as shown in Figure 2; hence, we did not obtain reliable stellar velocity dispersion measurements. Three of these objects that have black hole mass measurements from reverberation mapping were observed in the near-IR, and we determined stellar velocity dispersions for two of them as described in the next section.

3.2. Infrared Data

Because of the difficulty of measuring the stellar velocity dispersion in the optical, we obtained near-IR spectra for three galaxies with reverberation black hole masses (NGC 4748, Mrk 766, and Mrk 142) using OSIRIS. We also observed several velocity template stars with K and M spectral types. As noted by other studies (e.g., Watson et al. 2008), M giant stars give better fits compared to K giants since M giants are the representative stellar population in the near-IR bands. After experimenting with various spectral type velocity templates, we decided to use M1III and M2III stars for velocity dispersion measurements and took the mean as the final measurement with an uncertainty given by the quadrature sum of the fitting error and the rms scatter of results obtained from different templates. Figure 3 shows the observed galaxy spectra compared with the best-fit template. NGC 4748 shows a relatively good fit, while Mrk 766 presents stronger residuals due to template mismatch. All major *H*-band stellar lines, such as Mg I 1.488 μm, Mg I 1.503 μm, CO(3–0) 1.558 μm, CO(4–1) 1.578 μm, Si I 1.589 μm, and CO(5–2) 1.598 μm, are present in both objects. In the case of Mrk 142, which is fainter and at higher redshift than the other two objects, stellar absorption lines cannot be clearly identified and we could not obtain a reliable template fit or velocity dispersion measurement.

3.3. Previous Velocity Dispersion Measurements

Several objects in the LAMP sample have pre-existing velocity dispersion measurements in the literature. In most cases, the published results have fairly large uncertainties. Here, we briefly summarize the previous measurements and describe the available spectroscopic data from the Sloan Digital Sky Survey (SDSS).

SBS 1116+583A. Greene & Ho (2006) measured $\sigma = 50.3 \pm 18.0$ km s^{-1} using the SDSS spectrum. However, the velocity dispersion was not clearly resolved by the SDSS data, which have an instrumental dispersion of ~ 70 km s^{-1}.

Arp 151. Greene & Ho (2006) measured $\sigma = 124 \pm 12$ km s^{-1} from the SDSS spectrum.

Mrk 1310. Using the SDSS data, Greene & Ho (2006) reported $\sigma = 50 \pm 16$ km s^{-1}, which is below the resolution limit of the SDSS spectrum.

Mrk 202. Greene & Ho (2006) measured $\sigma = 85.6 \pm 14$ km s^{-1} from the SDSS spectrum.

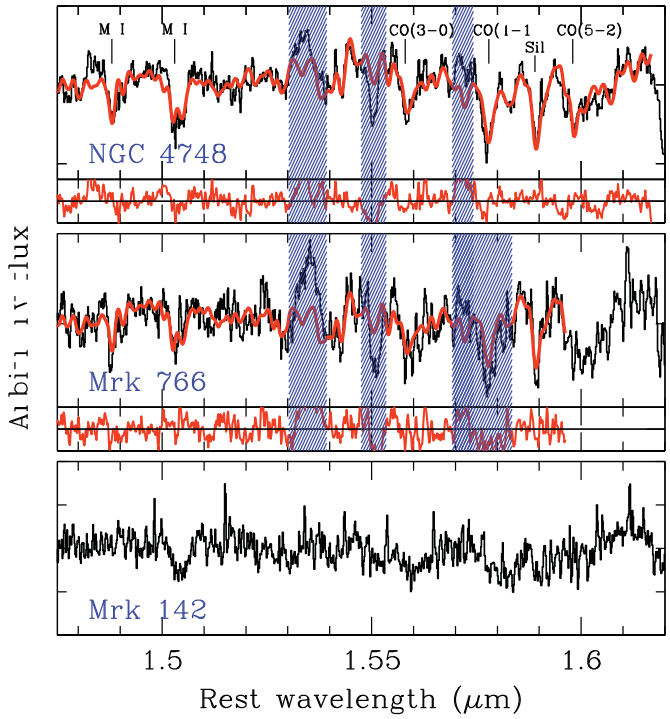

Figure 3. Velocity dispersion measurements using the OSIRIS spectra. The region including the main stellar features is shown together with the best-fit template (thick red line). Individual stellar lines are identified in the first panel. The regions around narrow AGN emission lines and regions of severe template mismatch, identified by shaded bands, are masked out before fitting. Residuals from the fit are shown at the bottom of NGC 4748 and Mrk 766.

(A color version of this figure is available in the online journal.)

Mrk 290. In the SDSS spectrum, the Ca II triplet lines are only weakly detected, and they appear to be badly contaminated by Ca II emission. The blue region of the spectrum is too dominated by the AGN for any stellar features to be clearly visible.

NGC 4253 (Mrk 766). Botte et al. (2005) reported a dispersion of $\sigma = 81 \pm 17$ km s^{-1} from the Ca II triplet lines. However, the Ca II triplet region is moderately contaminated by emission lines. Their dispersion measurements were carried out by cross-correlating the galaxy spectrum with that of a template star. Without a direct fit of the broadened template star to the galaxy spectrum, it is not clear how badly the measurement may be affected by the emission-line contamination.

An SDSS spectrum of Mrk 766 exists, but it appears to have been taken with the SDSS fiber positioned about 3″ away from the galaxy nucleus. Since the SDSS fiber missed the galaxy nucleus, the spectrum appears similar to that of a Seyfert 2 galaxy, dominated by starlight and with very weak broad components to the Balmer lines. Our own data from the Lick monitoring campaign, on the other hand, show a strongly AGN-dominated spectrum with much more prominent broad lines. Thus, while the Ca II triplet and other stellar absorption lines are clearly detected in the SDSS data, the offset position of the SDSS spectrum means that it should not be used to infer the bulge velocity dispersion.

NGC 5548. The most recent measurements of the velocity dispersion for this galaxy include $\sigma = 180 \pm 6$ km s^{-1} (Ferrarese et al. 2001) and $\sigma = 201 \pm 12$ km s^{-1} (Nelson et al. 2004).

NGC 6814. Nelson & Whittle (1995) listed a velocity dispersion of 115 ± 18 km s^{-1}.

Mrk 142. The SDSS spectrum of Mrk 142 (SDSS J102531.28+514034.8) shows that the object is strongly AGN dominated, and the stellar Ca II triplet lines are severely contaminated by Ca II emission. In addition, the spectral region around Mg *b* and Fe 5270 is completely dominated by strong Fe II emission, precluding any possibility of measuring the stellar velocity dispersion in the optical.

MCG −6-30-15. Oliva et al. (1999) measured $\sigma = 159$ km s^{-1} from template fits to the CO and Si features in the *H* band, but they did not list estimates of the measurement uncertainties. McHardy et al. (2005) used a spectrum around the Ca II triplet to measure $\sigma = 93.5 \pm 8.5$ km s^{-1}, using a cross-correlation technique.

All of the previous measurements with sufficiently high instrumental resolution are consistent with our new measurements within the errors, except for one object, MCG −6-30-15. The previously reported Ca II-based velocity dispersion and the *H*-band velocity dispersion of MCG −6-30-15 are dramatically different, and our measured dispersion based on the Ca II triplet is significantly lower than either previous result. Unfortunately, we cannot determine the origin of the discrepancy other than noting that the Ca II dispersion from McHardy et al. (2005) was determined using a cross-correlation method, and therefore it is not easy to directly compare the quality of the result with our measurement. As an additional check, we carried out an independent measurement of σ_* from the Palomar DBSP data using the template-fitting code of Barth et al. (2002). This gave $\sigma_* = 75 \pm 5$ km s^{-1}, consistent with the value of 76 ± 3 km s^{-1} measured with the van der Marel (1994) code. Since MCG −6-30-15 is not included in the $M_{\rm BH}$–σ_* relation analysis in the next section, this does not affect our main conclusions.

4. THE $M_{\rm BH}$–σ_* RELATION OF ACTIVE GALAXIES

The $M_{\rm BH}$–σ_* relation is expressed as

$$\log(M_{\rm BH}/M_\odot) = \alpha + \beta \log(\sigma_*/200\ {\rm km\ s^{-1}}). \quad (2)$$

For a sample of quiescent galaxies for which the sphere of influence of the black hole is spatially resolved in stellar or gas kinematics studies, Ferrarese & Ford (2005) measured $\alpha = 8.22 \pm 0.06$ and $\beta = 4.86 \pm 0.43$ with no evidence for intrinsic scatter. Using a larger sample, including late-type galaxies, Gültekin et al. (2009) recently reported $\alpha = 8.12 \pm 0.08$ and $\beta = 4.24 \pm 0.41$ with an intrinsic scatter $\sigma_{\rm int} = 0.44 \pm 0.06$.

In this section, we investigate the $M_{\rm BH}$–σ_* relation of active galaxies, by combining our eight new velocity measurements of the LAMP sample with 16 existing measurements of reverberation black hole mass and velocity dispersion taken from the literature. The relevant properties of the resulting sample of 24 AGNs are listed in Table 2, along with the original references for the measurements. Note that the selection bias investigated by Lauer et al. (2007) is not relevant to these reverberation objects since the bias mainly affects black holes in high-mass galaxies where the host-galaxy luminosity function is steeply falling.

As a first step, we determine the slope of the $M_{\rm BH}$–σ_* relation (Section 4.1) assuming that the virial coefficient *f* is unknown but does not depend on black hole mass. We also determine the intrinsic scatter in the relation. Then in Section 4.2, we determine the mean value and intrinsic scatter of the virial coefficient *f* by assuming that the slope and zero point of the $M_{\rm BH}$–σ_* relation are the same for active and quiescent galaxies. Note that in the following analysis the virial coefficient *f* and the zero point α are degenerate; therefore, additional information is needed to determine what fraction of the intrinsic scatter is due to *f* and how much is due to α, as we discuss below.

Table 2
Black Hole Masses and Stellar Velocity Dispersions

Galaxy	VP ($\sigma_{line}^2 R_{BLR}/G$) ($10^6\ M_\odot$)	VP Ref.	σ_* (km s^{-1})	Error	σ_* Ref.	log $M_{BH}/M_\odot$
LAMP Sample						
Arp 151	$1.22^{+0.16}_{-0.22}$	5	118	4	This work	6.81 ± 0.12
IC 4218	...		93	4	This work	...
MCG −6-30-15	...		76	3	This work	...
Mrk 1310	$0.41^{+0.12}_{-0.13}$	5	84	5	This work	6.33 ± 0.17
Mrk 142	$0.40^{+0.12}_{-0.14}$	5	...	...		6.32 ± 0.17
Mrk 202	$0.26^{+0.13}_{-0.10}$	5	78	3	This work	6.13 ± 0.22
NGC 4253 (Mrk 766)	$0.32^{+0.21}_{-0.20}$	5	93	32	This work	6.23 ± 0.30
NGC 4748	$0.47^{+0.16}_{-0.21}$	5	105	13	This work	6.39 ± 0.20
NGC 5548	$11.9^{+0.46}_{-0.46}$	6	195	13	This work	7.80 ± 0.10
NGC 6814	$3.36^{+0.54}_{-0.56}$	5	95	3	This work	7.25 ± 0.12
SBS 1116+583A	$1.05^{+0.33}_{-0.29}$	5	92	4	This work	6.74 ± 0.16
Previous Reverberation Sample						
Ark 120	$27.2^{+3.5}_{-3.5}$	1	221	17	1	8.15 ± 0.11
3C 120	$10.1^{+5.7}_{-4.1}$	1	162	20	2	7.72 ± 0.23
3C 390.3	$52.2^{+11.7}_{-11.7}$	1	273	16	1	8.44 ± 0.14
MRK 79	$9.52^{+2.61}_{-2.61}$	1	130	12	1	7.70 ± 0.16
MRK 110	$4.57^{+1.1}_{-1.1}$	1	91	7	3	7.38 ± 0.14
MRK 279	$6.35^{+1.67}_{-1.67}$	1	197	12	1	7.52 ± 0.15
MRK 590	$8.64^{+1.34}_{-1.34}$	1	189	6	1	7.66 ± 0.12
MRK 871	$8.98^{+1.4}_{-1.4}$	1	120	15	1	7.67 ± 0.12
NGC 3227	$7.67^{+3.9}_{-3.9}$	1	136	4	1	7.60 ± 0.24
NGC 3516	$7.76^{+2.65}_{-2.65}$	1	181	5	1	7.61 ± 0.18
NGC 3783	$5.42^{+0.99}_{-0.99}$	1	95	10	4	7.45 ± 0.13
NGC 4051	$.287^{+0.09}_{-0.12}$	2	89	3	1	6.18 ± 0.19
NGC 4151	$8.31^{+1.04}_{-0.85}$	3	97	3	1	7.64 ± 0.11
NGC 4593	$1.78^{+0.38}_{-0.38}$	4	135	6	1	6.97 ± 0.14
NGC 7469	$2.21^{+0.25}_{-0.25}$	1	131	5	1	7.06 ± 0.11
PG 1426+015	236^{+70}_{-70}	1	217	15	5	9.09 ± 0.16

Notes. Column 1: galaxy name. Column 2: virial product ($M_{BH}=f\times$VP) based on the line dispersion (σ_{line}) from reverberation mapping. Column 3: reference for virial product—(1) Peterson et al. 2004; (2) Denney et al. 2009b; (3) Bentz et al. 2006; (4) Denney et al. 2006; (5) Bentz et al. 2009b; (6) weighted mean of Bentz et al. 2007 and Bentz et al. 2009b. Column 4: stellar velocity dispersion. Column 5: error of stellar velocity dispersion. Column 6: reference for stellar velocity dispersion—(1) Nelson et al. 2004; (2) Nelson & Whittle 1995; (3) Ferrarese et al. 2001; (4) Onken et al. 2004; (5) Watson et al. 2008. Column 7: black hole mass calculated assuming the virial coefficient, $\log f = 0.72 \pm 0.10$. The uncertainty in the black hole mass is calculated by adding in quadrature the measurement uncertainty of the virial product in logarithmic space and the uncertainty in the virial coefficient (0.1 dex) as $\epsilon \log M_{BH} = \sqrt{\epsilon \mathrm{VP}^2/(\mathrm{VP} \ln 10)^2 + 0.1^2}$. The average of the positive and negative errors on the virial product is taken as the symmetric error (ϵVP).

4.1. The Slope

Active galaxies appear to obey an M_{BH}–σ_* relation with a slope consistent with that of quiescent galaxies (e.g., Gebhardt et al. 2000b; Ferrarese et al. 2001). However, the slope has not been well determined so far, because of limitations in sample size and in the dynamic range of M_{BH} for active galaxies with reverberation and stellar velocity dispersion measurements. The local AGN samples with single-epoch black hole masses selected from the SDSS are much larger than the reverberation sample (e.g., Greene & Ho 2006; Woo et al. 2008), but these mass estimates have larger uncertainties (∼0.5 dex) and may suffer from unknown systematic errors (Collin et al. 2006).

By adding our LAMP galaxies to the previous reverberation sample, we significantly increase the sample size, particularly at low-mass scales ($M_{BH} < 10^7\ M_\odot$), and extend the dynamic range to almost three decades in M_{BH}. This enables substantial progress in determining the slope of the M_{BH}–σ_* relation, independently for active galaxies. One important caveat is that the virial coefficient f may vary across the sample. Unfortunately, with existing data we cannot constrain the virial coefficient of each object. Therefore, in the analysis presented here we will assume that f is independent of black hole mass, although we allow for intrinsic scatter at fixed black hole mass. In the next section, we will take the opposite viewpoint and assume that the slope is known from quiescent samples when we investigate the intrinsic scatter in f and its dependence on M_{BH} and AGN properties.

In practice, our observable is the so-called virial product $\mathrm{VP} \equiv \sigma_{line}^2 R_{BLR}/G$, which is assumed to be related to the

black hole mass by a constant virial coefficient $M_{\rm BH}=f\times{\rm VP}$. Substituting into Equation (2), one obtains

$$\log {\rm VP} = \alpha + \beta\ \log\left(\frac{\sigma_*}{200\ {\rm km\ s^{-1}}}\right) - \log f. \quad (3)$$

In order to determine the slope β of the relation, we compute the posterior distribution function P. Assuming uniform priors on the parameters $\alpha' = \alpha - \log f$, β, and intrinsic scatter $\sigma_{\rm int}$, the posterior is equal to the likelihood given by

$$-2\ln P \equiv \sum_{i=1}^{N} \frac{\left[\log {\rm VP}_i - \alpha' - \beta \log\left(\frac{\sigma_*}{200}\right)_i\right]^2}{\epsilon_{{\rm tot},i}^2} + 2\ln\sqrt{2\pi\epsilon_{{\rm tot},i}^2}, \quad (4)$$

where

$$\epsilon_{{\rm tot},i}^2 \equiv \epsilon_{\log {\rm VP}_i}^2 + \beta^2\epsilon_{\log\sigma_* i}^2 + \sigma_{\rm int}^2, \quad (5)$$

and $\epsilon_{\log {\rm VP}}$ is the error on the logarithm of the virial product ($= \epsilon_{\rm VP}/({\rm VP}\ln 10)$) using the average of the positive and negative errors on the virial product as $\epsilon_{\rm VP}$, $\epsilon_{\log\sigma_*}$ is the error on the logarithm of the stellar velocity dispersion ($= \epsilon_{\sigma_*}/(\sigma_*\ln 10)$), and $\sigma_{\rm int}$ is the intrinsic scatter, which is treated as a free parameter. Note that our adopted likelihood is equivalent to that adopted as default by Gültekin et al. (2009) for their maximum likelihood analysis (see their Appendix A.2), with the inclusion of an additional Gaussian term to describe the uncertainties in velocity dispersion. After marginalizing over the other variables, the one-dimensional posterior distribution functions yield the following estimates of the free parameters: $\alpha' = 7.28 \pm 0.14$, $\beta = 3.55 \pm 0.60$, and $\sigma_{\rm int} = 0.43 \pm 0.08$.

To facilitate comparison with earlier studies (e.g., Tremaine et al. 2002), we also determine the slope with a "normalized" χ^2 estimator defined as

$$\chi^2 \equiv \sum_{i=1}^{N} \frac{\left[\log {\rm VP}_i - \alpha' - \beta \log\left(\frac{\sigma_*}{200}\right)_i\right]^2}{\epsilon_{{\rm tot},i}^2}, \quad (6)$$

where the intrinsic scatter $\sigma_{\rm int} = 0.43$ is set to yield χ^2 per degree of freedom equal to unity. The best estimate of the slope based on this normalized χ^2 estimator is $\beta = 3.72^{+0.40}_{-0.39}$. If we assume no intrinsic scatter, then the best-fit slope becomes slightly steeper as $\beta = 3.97^{+0.13}_{-0.13}$. However, confirming our previous result based on a full posterior analysis, the intrinsic scatter cannot be negligible since the χ^2 per degree of freedom would be much larger than unity ($\sim$14) if the intrinsic scatter is assumed to be zero.

These results indicate that the slopes of the $M_{\rm BH}$–σ_* relation for active and quiescent galaxies are consistent within the uncertainties. The total intrinsic scatter is 0.43 ± 0.08 dex, which is a combination of the scatter of the $M_{\rm BH}$–σ_* relation and that of the virial coefficient. Without additional information, we cannot separate the contribution of the intrinsic scatter on the virial coefficient (i.e., the diversity of BLR kinematic structure among AGN) from the intrinsic scatter in black hole mass at fixed velocity dispersion (i.e., the diversity of black hole masses among galaxies). We will address this issue in Section 4.2.

4.2. The Virial Coefficient

In order to transform the virial product into an actual black hole mass, we need to know the value of the virial coefficient f. Our current understanding of the geometry and kinematics of the BLR is insufficient to compute f from first principles. This creates a systematic uncertainty in the determination of black hole mass from reverberation mapping. As an example, if a spherical isotropic velocity distribution is assumed, then the velocity dispersion of the gas is a factor of $\sqrt{3}$ larger than the measured line-of-sight velocity dispersion ($\sigma_{\rm line}$), hence a value of $f = 3$ is often assumed for a spherically symmetric BLR (e.g., Wandel et al. 1999; Kaspi et al. 2000). If, instead, the BLR is described by a circular rotating disk, then the value of f can be a few times larger than the isotropic case, depending on the inclination angle and the scale height of the disk (see Collin et al. 2006 for more details).

As mentioned above, determining the virial coefficient for individual AGNs is not feasible due to the limited spatial resolution of the current and foreseeable future instruments since the angular size of the BLR is microarcseconds. Therefore, in practice, an average virial coefficient is usually determined by assuming that local Seyfert galaxies and quasar host galaxies follow the same $M_{\rm BH}$–σ_* relation (Onken et al. 2004) and deriving the appropriate value for f. Using this method, Onken et al. (2004) measured $\langle f\rangle = 5.5 \pm 1.8$ based on a sample of 14 reverberation-mapped Seyfert galaxies with measured stellar velocity dispersions.

In this section, we apply the same methodology to our enlarged sample to determine the average value of f as well as the intrinsic scatter, assuming the intercept (α) and slope (β) of the $M_{\rm BH}$–σ_* relation for quiescent galaxies. In practice, we modify the likelihood given in Equation (4) by fixing the slope and intercept to the values obtained by two independent groups, Ferrarese & Ford (2005) and Gültekin et al. (2009). Figures 4 and 5 show the best-fit $M_{\rm BH}$–σ_* relations for the enlarged reverberation sample, respectively, assuming the quiescent $M_{\rm BH}$–σ_* relation from Ferrarese & Ford (2005) and that from Gültekin et al. (2009). Adopting the $M_{\rm BH}$–σ_* relation of Ferrarese & Ford (2005; $\alpha = 8.22$ and $\beta = 4.86$), we determine $\log f = 0.71 \pm 0.10$ and $\sigma_{\rm int} = 0.46^{+0.07}_{-0.09}$ dex. Adopting the $M_{\rm BH}$–σ_* relation from Gültekin et al (2009; $\alpha = 8.12$ and $\beta = 4.24$), we obtain $\log f = 0.72^{+0.09}_{-0.10}$ and $\sigma_{\rm int} = 0.44 \pm 0.07$. The average values are in good agreement with $f = 5.5 \pm 1.8$ (i.e., $\log f = 0.74^{+0.10}_{-0.13}$) as found by Onken et al. (2004). The average value is inconsistent with that expected for a spherical BLR ($f = 3$), and closer to that expected for a disk-like geometry, although there may be a diversity of geometries and large-scale kinematics (e.g., Bentz et al. 2009b; Denney et al. 2009a).

As discussed at the end of Section 4.1, the intrinsic scatter determined in this section is a combination of intrinsic scatter in f and in zero point of the $M_{\rm BH}$–σ_* relation (which are degenerate in Equation (4)). We need additional information to break this degeneracy. If the intrinsic scatter of the active galaxy $M_{\rm BH}$–σ_* relation were close to 0.31 dex (as determined for elliptical galaxies by Gültekin et al. 2009), then the residual intrinsic scatter of the virial coefficient would be 0.31 dex. In contrast, if the scatter of the $M_{\rm BH}$–σ_* relation of active galaxies were closer to 0.44 dex (as found for all galaxies by Gültekin et al. 2009), then the intrinsic scatter in f would be close to zero. Although we cannot break this degeneracy with current data, the bottom line is the same as far as determining black hole masses from reverberation-mapping data is concerned (and from single-epoch data, as a consequence). Since for the purpose of the calibration of f, the two sources of scatter are indistinguishable, the uncertainty in our calibration of f (whether it is due to diversity in BLR physics or diversity in the galaxy–AGN connection) is the largest remaining uncertainty in black hole mass determinations that rely on this technique.

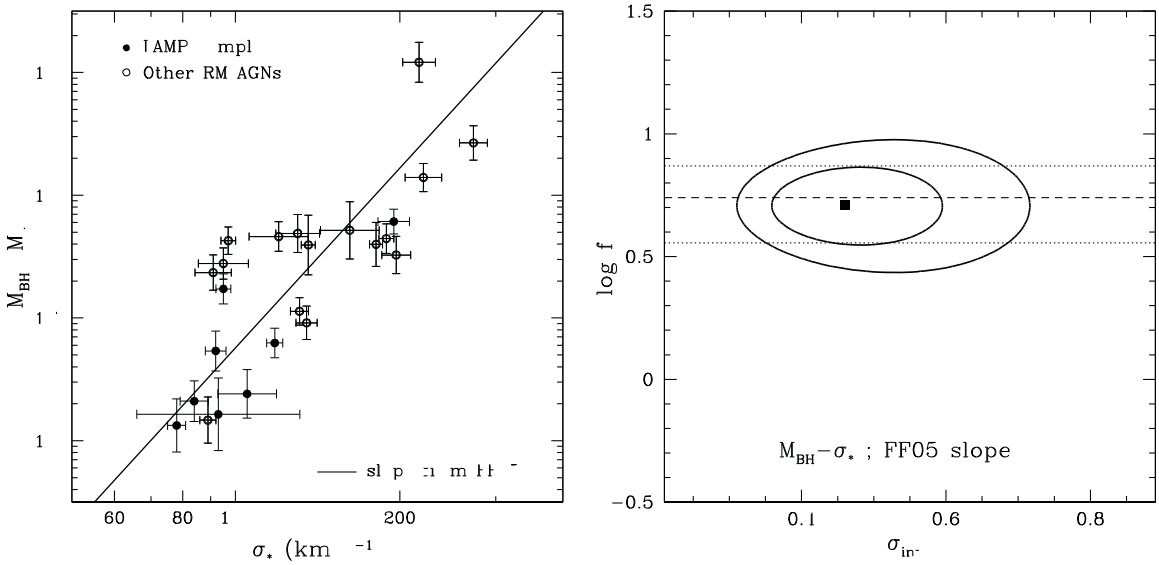

Figure 4. Left: M_{BH}–σ_* relation of the combined reverberation sample, adopting the slope from Ferrarese & Ford (2005) and the best-fit virial coefficient from this work. Right: posterior probability contour levels (68% and 95%) for the virial coefficient f and its intrinsic scatter, as determined assuming the slope from Ferrarese & Ford (2005). The horizontal lines represent the previous estimate from Onken et al. (2004; dashed line) with its 68% uncertainties (dotted lines).

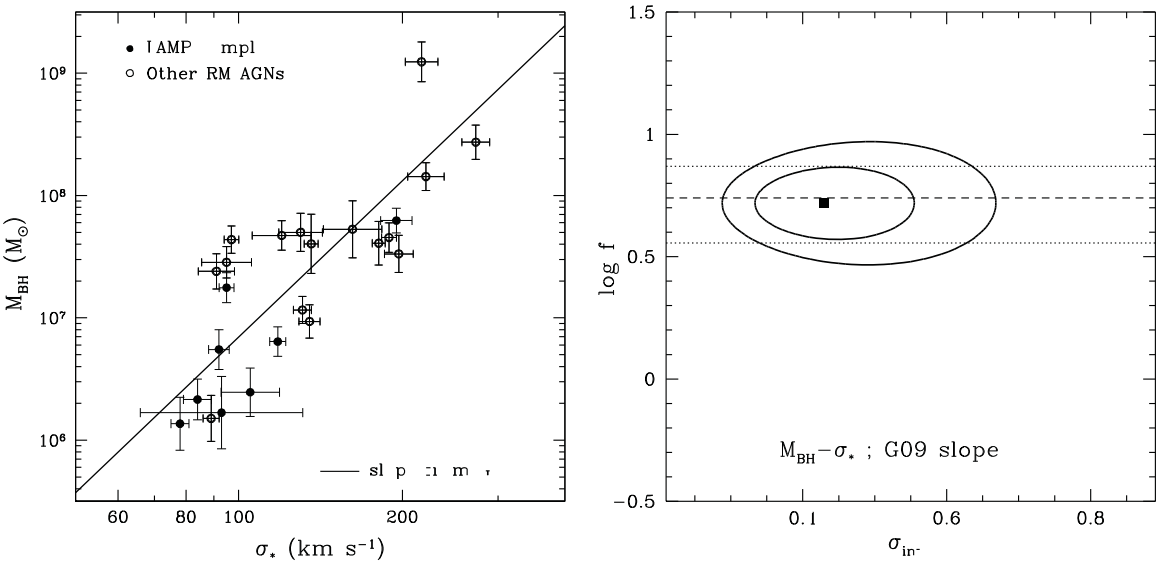

Figure 5. As in Figure 4, but adopting the slope from Gültekin et al. (2009).

To investigate any dependence of the virial coefficient on AGN properties, we collected from the literature the Hβ line widths (V_{FWHM} and σ_{line}) and the optical AGN luminosities for reverberation-mapped AGNs, corrected for the host-galaxy contribution (Peterson et al. 2004; Bentz et al. 2009a). When multiple luminosity measurements are available for given objects, we used the weighted mean of the luminosity (Table 9 of Bentz et al. 2009a). For the seven LAMP objects with M_{BH} and velocity dispersion measurements, *Hubble Space Telescope* imaging is not yet available for measuring the starlight correction to the spectroscopic luminosity. Thus, we inferred the AGN luminosity from the measured time lag using the size–luminosity relation (Bentz et al. 2009a). The bolometric luminosity was calculated by multiplying the optical AGN luminosity by a factor of 10 (Woo & Urry 2002), and we assumed 0.3 dex error in the Eddington ratio.

In Figure 6, we plot the residuals from the M_{BH}–σ_* relation with $\alpha = 8.12$, $\beta = 4.24$ taken from Gültekin et al. (2009), and $\log f = 0.72$ as determined in Section 6.2. The residuals were determined as $\Delta \log M_{BH} = \log \mathrm{VP} + \log \mathrm{f} - (\alpha + \beta \log \sigma_*)$. To test for potential correlations between residuals and line properties or Eddington ratios, we fit each data set with a straight line by minimizing the normalized χ^2 estimator. We find no dependence of the residuals on the line width (either V_{FWHM} or σ_{line}). In the case of the Eddington ratio, we find a weak dependence with a non-zero slope ($-2.3^{+0.6}_{-1.1}$), significant at the 95% level; however, this weak trend is mainly due to one object with the lowest Eddington ratio in the sample. When we remove that object, the best-fit slope becomes consistent with no correlation. Further investigation using a larger sample, evenly distributed over the range of the Eddington ratio, is required to better constrain the residual dependence on the Eddington ratio. In the case of the line width, it is not straightforward to test

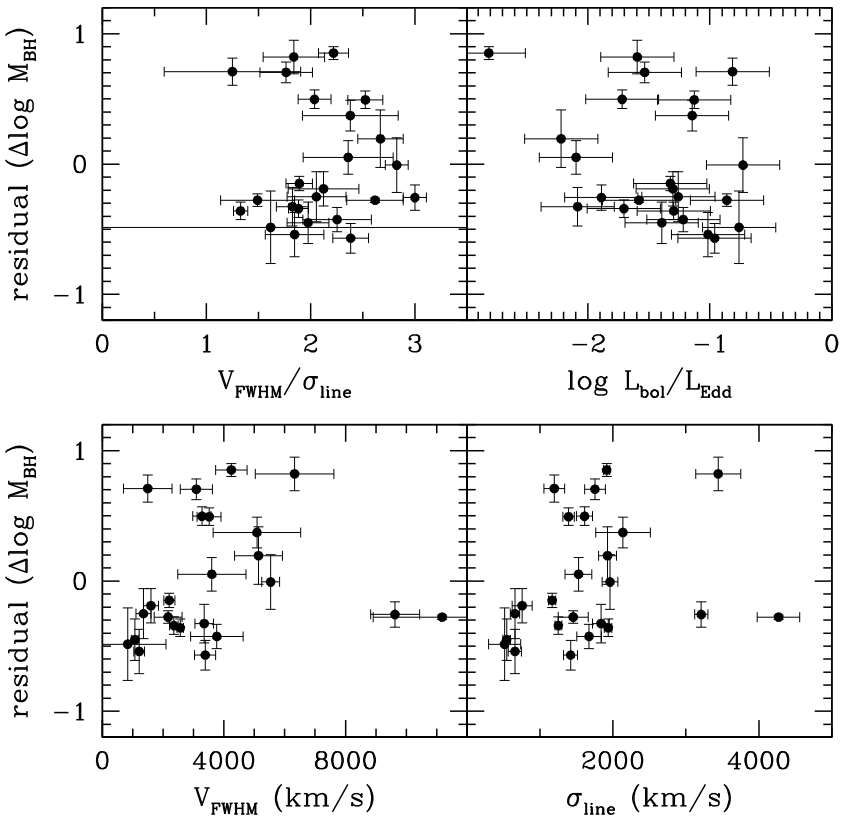

Figure 6. Dependence of residuals from the $M_{\rm BH}$–σ_* relation ($\Delta \log M_{\rm BH} = (\log {\rm VP} + \log f) - (\alpha + \beta \log \sigma/(200\ {\rm km\ s^{-1}}))$ on parameters related to the accretion state: $V_{\rm FWHM}/\sigma_{\rm line}$ (top left); Eddington ratio (top right); $V_{\rm FWHM}$ (bottom left); line dispersion $\sigma_{\rm line}$ (bottom right) of the Hβ line. In this plot, we adopt the local relation with $\alpha = 8.12$, $\beta = 4.24$ taken from Gültekin et al. (2009), and $\log f = 0.72$ as determined in Section 6.2.

the dependence since the line width of most of our objects is relatively small, $\sigma_{\rm line} < 2000$ km s^{-1}. By dividing our sample at $\sigma_{\rm line} = 1500$ km s^{-1} into two groups of similar sample size, we separately measured the virial coefficient for narrower-line and broader-line AGNs. The difference in the virial coefficient is $\Delta \log f = 0.1$–0.2, which is not significant given the uncertainty of 0.15 dex on the virial coefficient.

5. DISCUSSION

We present the $M_{\rm BH}$–σ_* relation of the reverberation sample in Figure 7, using the slope, $\beta = 3.55 \pm 0.60$, determined in Section 4.1 and the average virial coefficient, $\langle \log f \rangle = 0.72 \pm 0.10$, determined in Section 4.2. Compared to the local quiescent galaxies, active galaxies follow a consistent $M_{\rm BH}$–σ_* relation with a similar slope and scatter. Note that the mean black hole mass of the reverberation sample ($\langle \log M_{\rm BH}/M_\odot \rangle = 7.3 \pm 0.74$) is an order of magnitude smaller than that of quiescent galaxies ($\langle \log M_{\rm BH}/M_\odot \rangle = 8.2 \pm 0.79$). The slightly shallower slope of the reverberation sample is consistent with the trend in the quiescent galaxies that the slope is shallower for galaxies with lower velocity dispersion ($\sigma_* < 200$ km s^{-1}); see Gültekin et al. (2009). In contrast, the slope of late-type quiescent galaxies (4.58 ± 1.58) seems higher than the slope of our active galaxies, which are mainly late-type galaxies. However, given the uncertainty in the slope ($\beta = 3.55 \pm 0.60$) of the active galaxy $M_{\rm BH}$–σ_* relation, the difference between quiescent and active galaxies is only marginal. We did not attempt to divide our sample into various morphology groups or a few mass bins to test the dependence of the slope, since the sample size is still small and biased toward lower mass objects.

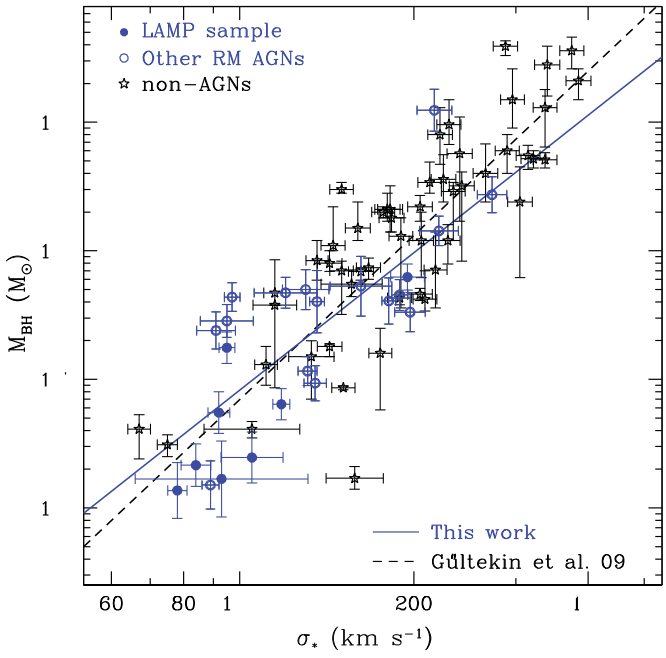

Figure 7. $M_{\rm BH}$–σ_* relation of active galaxies with reverberation black hole masses (blue), compared with non-active galaxies with dynamical black hole masses. The reverberation masses were determined assuming the virial coefficient, $\log f = 0.72 \pm 0.10$. The solid line is the best-fit slope of the active galaxies, while the dashed line is the best fit to the inactive galaxy samples from Gültekin et al. (2009).

(A color version of this figure is available in the online journal.)

The smaller mean M_{BH} of the reverberation sample is due to the relative difficulty of measuring the stellar velocity dispersions for the more luminous and higher redshift quasars that have the largest black hole masses. Although there are 17 quasars with measured reverberation black hole masses, the stellar velocity dispersions have not been measured for most of those high-luminosity objects (see Watson et al. 2008; Dasyra et al. 2007). In our current sample, there are only three objects above $3 \times 10^8\ M_\odot$. In order to better constrain the M_{BH}–σ_* relation of active galaxies, it will be necessary to pursue further measurements of velocity dispersions for reverberation-mapped AGNs at high masses. Additional stellar velocity dispersion measurements will be available based on Keck OSIRIS spectra in the near future (J.-H. Woo & M. A. Malkan 2010, in preparation).

The key assumption in determining the slope of the M_{BH}–σ_* relation is that the virial coefficient does not systematically vary as a function of black hole mass. Currently, we do not have sufficient information to test whether this assumption is valid. In an empirical study of the systematic effects of emission-line profiles, Collin et al. (2006) showed that it was necessary to use a smaller value of the virial coefficient for AGNs with larger V_{FWHM}. In contrast, the change of the virial coefficient was not required if the line dispersion (σ_{line}) was used instead. These results reflect the fact that there is a large range of V_{FWHM}/σ_{line} ratio, and that systematic uncertainties are higher if V_{FWHM} is used.

With the enlarged sample of 24 AGNs, we investigated the dependence of the virial coefficient on the line properties and the Eddington ratio. However, we did not clearly detect any increasing trend of the intrinsic scatter with the line profile, line width, or Eddington ratio, implying that the M_{BH} based on the mean virial coefficient is not systematically over- or underestimated as a function of line width or the Eddington ratio. We note that since our sample is still small and biased to narrower-line and lower Eddington ratio objects, further investigation with a larger sample, particularly at higher mass scales, is required to better constrain the systematic errors.

For single-epoch black hole mass determination, we suggest using $\log f = 0.72 \pm 0.10$ when the gas velocity is determined from the line dispersion (σ_{line}). If the FWHM of an emission line (V_{FWHM}) is measured instead of the line dispersion, then additional information on the V_{FWHM}/σ_{line} ratio will be needed in the black hole mass calculation. The value of V_{FWHM}/σ_{line} is typically assumed to be 2 (Netzer 1990), although there is a range of values. For example, the mean of V_{FWHM}/σ_{line} of our reverberation sample is 2.09 with a standard deviation of 0.45 (also see Peterson et al. 2004 and McGill et al. 2008). We did not attempt to determine an average virial coefficient using the virial product based on V_{FWHM}. A correction factor depending on V_{FWHM}/σ_{line} should be applied in addition to the virial coefficient, $\log f = 0.72$, when gas velocity is determined from V_{FWHM}. Our empirical measurement of the mean virial coefficient is not very different from that of Onken et al. (2004), although the sample size and the dynamical range of the reverberation sample is significantly improved.

We note that our results on the mean virial coefficient are based on broad-line dispersions measured from the rms spectra, which are not generally available for single-epoch black hole mass determinations. Detailed comparison of broad-line profiles and widths between rms and single-epoch spectra is necessary to understand the additional uncertainty of single-epoch black hole mass estimates (see Denney et al. 2009a), and we will pursue further investigations of this issue using LAMP data in the future.

6. SUMMARY

We summarize the main results as follows.

1. Using the high S/N optical and near-IR spectra obtained at the Keck, Palomar, and Lick Observatories, we measured the stellar velocity dispersion of 10 local Seyfert galaxies, including 7 objects (SBS 1116+ 583A, Arp 151, Mrk 1310, Mrk 202, NGC 4253, NGC 4748, and NGC 6814) with newly determined reverberation black hole masses from the LAMP project (and NGC 5548, IC 4218, and MCG −6-30-15).
2. For a total sample of 24 local AGNs, combining our new stellar velocity dispersion measurements of the LAMP sample and the previous reverberation sample with the stellar velocity dispersion from the literature, we determined the slope and the intrinsic scatter of the M_{BH}–σ_* relation in the range of black hole mass $10^6 < M_{BH}/M_\odot < 10^9$. The best-fit slope is $\beta = 3.55 \pm 0.60$, consistent within the uncertainty with the slope of quiescent galaxies. The intrinsic scatter, 0.43 ± 0.08 dex, of active galaxies is also similar to that of quiescent galaxies. Thus, we find no evidence for dependence of the present-day M_{BH}–σ_* relation slope on the level of activity of the central black hole.
3. We determined the virial coefficient using the slope and the intercept of the M_{BH}–σ_* relation of quiescent galaxies, taken from two groups (Ferrarese & Ford 2005; Gültekin et al. 2009). The best-fit virial coefficient ($\log f$) is 0.71 ± 0.10 ($0.72^{+0.09}_{-0.10}$) with an intrinsic scatter, $0.46^{+0.07}_{-0.09}$ (0.44 ± 0.07) with the slope, 4.86 (4.24) taken from Ferrarese & Ford (Gültekin et al. 2009). We take $f = 5.2$ (i.e., $\log f = 0.72$) as the best value of the mean virial coefficient, which is a factor of ∼1.7 larger than the standard factor obtained for isotropic spatial and velocity distribution. The substantial intrinsic scatter indicates that the virial coefficient is the main source of uncertainties in determining black hole masses, either using reverberation mapping or single-epoch spectra.

J.H.W. acknowledges support from Seoul National University by the Research Settlement Fund for new faculty, and support from NASA through Hubble Fellowship grant HF-51249 awarded by the Space Telescope Science Institute. T.T. acknowledges support from the NSF through CAREER award NSF-0642621, by the Sloan Foundation through a Sloan Research Fellowship, and by the Packard Foundation through a Packard Fellowship. Research by A.J.B. and A.V.F. is supported by NSF grants AST-0548198 and AST-0908886, respectively. The work of D.S. was carried out at the Jet Propulsion Laboratory, California Institute of Technology, under a contract with NASA. Research by G.C. is supported by NSF grant AST-0507450. We thank the referee for useful suggestions.

Data presented herein were obtained at the W. M. Keck Observatory, which is operated as a scientific partnership among Caltech, the University of California, and NASA; it was made possible by the generous financial support of the W. M. Keck Foundation. The authors wish to recognize and acknowledge the very significant cultural role and reverence that the summit of Mauna Kea has always had within the indigenous Hawaiian community; we are most fortunate to have the opportunity to conduct observations from this mountain. We are grateful for the assistance of the staffs at the Keck, Palomar, and Lick Observatories. We thank Kartik Sheth for assisting with some of the Palomar observations. We acknowledge the use of the

HyperLeda database (http://leda.univ-lyon1.fr). This research has made use of the NASA/IPAC Extragalactic Database (NED) which is operated by the Jet Propulsion Laboratory, California Institute of Technology, under contract with the National Aeronautics and Space Administration.

REFERENCES

Barth, A. J., Ho, L. C., & Sargent, W. L. W. 2002, AJ, 124, 2607
Bennert, V. N., et al. 2010, ApJ, 708, 1507
Bentz, M. C., Peterson, B. M., Netzer, H., Pogge, R. W., & Vestergaard, M. 2009a, ApJ, 697, 160
Bentz, M. C., et al. 2006, ApJ, 651, 775
Bentz, M. C., et al. 2007, ApJ, 662, 205
Bentz, M. C., et al. 2009b, ApJ, 705, 199
Bentz, M. C., et al. 2010, ApJ, in press (arXiv:1004.2922)
Botte, V., Ciroi, S., di Mille, F., Rafanelli, P., & Romano, A. 2005, MNRAS, 356, 789
Collin, S., Kawaguchi, T., Peterson, B. M., & Vestergaard, M. 2006, A&A, 456, 75
Davies, R. I. 2007, MNRAS, 375, 1099
Dasyra, K. M., et al. 2007, ApJ, 657, 102
Denney, K. D., et al. 2006, ApJ, 653, 152
Denney, K. D., Peterson, B. M., Dietrich, M., Vestergaard, M., & Benz, M. C. 2009a, ApJ, 692, 246
Denney, K. D., et al. 2009b, ApJ, 702, 1353
Ferrarese, L., & Merritt, D. 2000, ApJ, 539, L9
Ferrarese, L., & Ford, H. 2005, Space Sci. Rev., 116, 523
Ferrarese, L., Pogge, R. W., Peterson, B. M., Merritt, D., Wandel, A., & Joseph, C. L. 2001, ApJ, 555, L79
Filippenko, A. V. 1982, PASP, 94, 715
Gebhardt, K., et al. 2000a, ApJ, 539, L13
Gebhardt, K., et al. 2000b, ApJ, 543, L5
Greene, J. E., & Ho, L. C. 2006, ApJ, 641, 117
Gültekin, K., et al. 2009, ApJ, 698, 198
Horne, K. D. 1986, PASP, 98, 609
Jahnke, K., et al. 2009, ApJ, 706, L215
Kaspi, S., Maoz, D., Netzer, H., Peterson, B. M., Vestergaard, M., & Jannuzi, B. T. 2005, ApJ, 629, 61
Kaspi, S., Smith, P. S., Netzer, H., Maoz, D., Jannuzi, B. T., & Giveon, U. 2000, ApJ, 533, 631
Kormendy, J. 2004, in Carnegie Obs. Centennial Symp., Coevolution of Black Holes and Galaxies, ed. L. C. Ho (Cambridge: Cambridge Univ. Press), 1
Krabbe, A., Gasaway, T., Song, I., Iserlohe, C., Weiss, J., Larkin, J. E., Barczys, M., & Lafreniere, D. 2004, Proc. SPIE, 5492, 1403
Larkin, J., et al. 2006, New Astron. Rev., 50, 362
Lauer, T. R., Tremaine, S., Richstone, D., & Faber, S. M. 2007, ApJ, 670, 249
Marconi, A., Axon, D. J., Maiolino, R., Nagao, T., Pastorini, G., Pietrini, P., Robinson, A., & Torricelli, G. 2008, ApJ, 678, 693
McGill, K. L., Woo, J.-H., Treu, T., & Malkan, M. A. 2008, ApJ, 673, 703
McHardy, I. M., Gunn, K. F., Uttley, P., & Goad, M. R. 2005, MNRAS, 359, 1469
McLure, R. J., & Dunlop, J. S. 2004, MNRAS, 352, 1390
McLure, R. J., & Jarvis, M. J. 2002, MNRAS, 337, 109
Merloni, A., et al. 2010, ApJ, 708, 137
Miller, J. S., & Stone, R. P. S. 1993, Lick Obs. Tech. Rep. 66 (Santa Cruz, CA: Univ. California)
Nelson, C. H., Green, R. F., Bower, G., Gebhardt, K., & Weistrop, D. 2004, ApJ, 615, 652
Nelson, C. H., & Whittle, M. 1995, ApJS, 99, 67
Netzer, H. 1990, in Active Galactic Nuclei, ed. T. J.-L. Courvoisier & M. Major (Berlin: Springer), 57
Netzer, H., Lira, P., Trakhtenbrot, B., Shemmer, O., & Cury, I. 2007, ApJ, 671, 1256
Oke, J. B., & Gunn, J. E. 1982, PASP, 94, 586
Oliva, E., Origlia, L., Maiolino, R., & Moorwood, A. F. M. 1999, A&A, 350, 9
Onken, C. A., et al. 2004, ApJ, 615, 645
Peng, C. Y., Impey, C. D., Ho, L. C., Barton, E. J., & Rix, H.-W. 2006a, ApJ, 640, 114
Peng, C. Y., Impey, C. D., Rix, H.-W., Kochanek, C. S., Keeton, C. R., Falco, E. E., Lehár, J., & McLeod, B. A. 2006b, ApJ, 649, 616
Peterson, B. M., et al. 2004, ApJ, 613, 682
Sand, D. J., Treu, T., Smith, G. P., & Ellis, R. S. 2004, ApJ, 604, 88
Sheinis, A. I., Bolte, M., Epps, H. W., Kibrick, R. I., Miller, J. S., Radovan, M. V., Bigelow, B. C., & Sutin, B. M. 2002, PASP, 114, 851
Shen, J., Vanden Berk, D. E., Schneider, D. P., & Hall, P. B. 2008, AJ, 135, 928
Tremaine, S., et al. 2002, ApJ, 574, 740
Treu, T., Malkan, M. A., & Blandford, R. D. 2004, ApJ, 615, L97
van Dam, M. A., et al. 2006, PASP, 118, 310
van Dam, M. A., Johansson, E., Stomski, P., Sumner, R., Chin, J., & Wizinowich, P. 2007, Keck Adaptive Optics Note 489, http://www2.keck.hawaii.edu/optics/aodocs/KAON489.pdf
van der Marel, R. P. 1994, MNRAS, 270, 271
Vestergaard, M. 2002, ApJ, 571, 733
Vestergaard, M., & Peterson, B. M. 2006, ApJ, 641, 689
Walsh, J. L., et al. 2009, ApJS, 185, 156
Wandel, A., Peterson, B. M., & Malkan, M. A. 1999, ApJ, 526, 579
Watson, L. C., Martini, P., Dasyra, K. M., Bentz, M. C., Ferrarese, L., Peterson, B. M., Pogge, R. W., & Tacconi, L. J. 2008, ApJ, 682, L21
Wizinowich, P. L., et al. 2006, PASP, 118, 297
Woo, J.-H., Treu, T., Malkan, M. A., & Blandford, R. D. 2006, ApJ, 645, 900
Woo, J.-H., Treu, T., Malkan, M. A., & Blandford, R. D. 2008, ApJ, 681, 925
Woo, J.-H., & Urry, C. M. 2002, ApJ, 579, 530
Woo, J.-H., Urry, C. M., Lira, P., van der Marel, R. P., & Maza, J. 2004, ApJ, 617, 903
Woo, J.-H., Urry, C. M., van der Marel, R. P., Lira, P., & Maza, J. 2005, ApJ, 631, 762